Development of a Ni–Ce$_{0.8}$Zr$_{0.2}$O$_2$ catalyst for solid oxide fuel cells operating on ethanol through internal reforming

Mingming Liao, Wei Wang, Ran Ran, Zongping Shao*

State Key Laboratory of Materials-Oriented Chemical Engineering, College of Chemistry & Chemical Engineering,
Nanjing University of Technology, No. 5 Xin Mofan Road, Nanjing 210009, PR China

ARTICLE INFO

ABSTRACT

Inexpensive 20 wt.% Ni–Ce$_{0.8}$Zr$_{0.2}$O$_2$ catalysts are synthesized by a glycine nitrate process (GNP) and an impregnation process (IMP). The catalytic activity for ethanol steam reforming (ESR) at 400–650 °C, catalytic stability and carbon deposition properties are investigated. Ni–Ce$_{0.8}$Zr$_{0.2}$O$_2$ (GNP) shows a higher catalytic performance than Ni–Ce$_{0.8}$Zr$_{0.2}$O$_2$ (IMP), especially at lower temperatures. It also presents a better coking resistance and a lower graphitization degree of the deposited carbon. The superior catalytic activity and coke resistance of Ni–Ce$_{0.8}$Zr$_{0.2}$O$_2$ (GNP) is attributed to the small particle size of the active metallic nickel phase and the strong interaction between the nickel and the Ce$_{0.8}$Zr$_{0.2}$O$_2$ support, as evidenced by the XRD and H$_2$-TPR. The Ni–Ce$_{0.8}$Zr$_{0.2}$O$_2$ (GNP) is further applied as an anode functional layer in solid oxide fuel cells operating on ethanol steam. The cell yields a peak power density of 536 mW cm^{-2} at 700 °C when operating on EtOH–H$_2$O gas mixtures, which is only slightly lower than that of hydrogen fuel, whereas the cell without the functional layer failed for short-term operations. Ni–Ce$_{0.8}$Zr$_{0.2}$O$_2$ (GNP) is promising as an active and highly coking-resistant catalyst layer for solid-oxide fuel cells operating on ethanol steam fuel.

1. Introduction

The expanding energy demands and shortage of petroleum reserves necessitate the development of alternative energy materials and technologies for a sustainable future. Fuel cells, electrochemical energy conversion devices that directly convert chemical energy into electric power with high efficiency and low emissions, have been proposed as a major energy source that may decrease the global reliance on fossil fuels and reduce greenhouse emissions. Ethanol is a good alternative renewable fuel, which can be obtained from biomass fermentation. Ethanol steam reforming (ESR) provides an environmentally friendly way to produce hydrogen for fuel cells [1,2], which is a cleaner process than methane steam reforming that contributes little to the green house effect because CO$_2$ can be consumed during the biomass growth which was so-called "CO$_2$-free" cycle.

Solid oxide fuel cells (SOFCs) are high-temperature fuel cells with fuel flexibility [3–7]. Recently, ethanol has attracted attention as a fuel for SOFCs. However, the direct operation of conventional SOFCs on ethanol could result in the quick degradation of cell performance due to the quick carbon build-up over the nickel cermet anode. The pre-reforming of ethanol to hydrogen is

a method for SOFCs to operate on ethanol fuel without the need for cell improvement. However, the external reforming process increases the system complexity on the one hand and decreases the overall efficiency on the other hand. The internal reforming of ethanol is a more preferable way for operating on ethanol fuel. Unfortunately, the highly sintered nickel cermet anode shows poor catalytic activity for the ethanol reforming reaction and displays easy coke formation. Recently, it has been demonstrated by several authors that SOFCs can be operated on hydrocarbon fuels directly or through internal reforming by simply modifying the conventional anode with a thin layer of catalyst that has high activity towards the hydrocarbon reforming reactions. For example, Zhan and Barnett were the first to demonstrate Ru–CeO$_2$ as such a catalyst [8]. The power output and anode coke resistance of fuel cells with a Ru–CeO$_2$ functional layer were much improved, as compared to the conventional cells without a catalyst layer when operating on methane, propane or octane fuels [8–10].

Some supported group VIII metals, including Ni, Cu, Co, Rh, Ru, Pd and Pt, are known to be good catalysts for ESR [11–15]; in particular, the supported noble metal catalysts have excellent catalytic activity. However, the high cost of those noble metals limits their large-scale application. The development of a less expensive catalytic system with high activity and stability will be an important aspect in making this technique economically competitive. As a low-cost and non-noble alternative, nickel-based catalysts have been widely used in hydrogenation and dehydrogenation reactions.

* Corresponding author. Tel.: +86 25 83172256; fax: +86 25 83172242.
E-mail address: shaozp@njut.edu.cn (Z. Shao).

Nickel-based catalysts have superior ESR activity because of their high performance for C–C rupture. Ni–Al$_2$O$_3$, as the most effective catalysts, have been applied for reforming methane with carbon dioxide, but they suffer from carbon deposition, nickel sintering and phase transformation [16–18]. Coke deposition is the main cause for the deactivation of Ni–Al$_2$O$_3$ catalysts during ESR. The routes for carbon formation include the Boudouard reaction, methane decomposition and polymerization of ethene; the latter originated from ethanol dehydration over Al$_2$O$_3$ acidic sites. The high oxygen storage capacity (OSC) of CeO$_2$ improves catalytic performance by storing oxygen under an oxidative atmosphere and releasing it under a reductive atmosphere [19,20]. The superiority in its promotion for the water–gas shift (WGS) reaction, thermal stability and oxygen storage capacity makes it a good additive in three-way catalyst (TWC) formulations [21]. According to the literature [22], doping CeO$_2$ with suitable cations, such as Zr^{4+}, Al^{3+} and Si^{4+}, can enhance the microstructural stability. Moreover, the characteristic feature of the valence shift between Ce^{4+} and Ce^{3+} allows it to easily obtain, release and transport oxygen in the CeO$_2$-based materials and, consequently, induces a high OSC. It has also been reported that the addition of ZrO$_2$ to CeO$_2$ leads to an improvement in the OSC, redox properties, and thermal resistance of CeO$_2$. In addition, this modification also increases the metal dispersion [20,23,24]. CeO$_2$–ZrO$_2$ was superior to Al$_2$O$_3$ for the ESR reaction because it can restrict ethylene formation, and the optimum CeO$_2$-to-ZrO$_2$ molar ratio in the Ce$_x$Zr$_{1-x}$O$_2$ series was found to be approximately 4:1 for hydrogen production [25,26].

In our previous work, we have demonstrated that the glycine nitrate process is a facile way to develop nanosized Ce$_x$Zr$_{1-x}$O$_2$ (x = 0.2, 0.4, 0.6 or 0.8). The Pt–Ce$_x$Zr$_{1-x}$O$_2$ catalysts, prepared via incipient-to-wetness impregnation, showed high activity for ethanol steam reforming [27].

In this work, a less expensive Ni–Ce$_{0.8}$Zr$_{0.2}$O$_2$ catalyst was synthesized for the application as an anode functional layer of SOFCs operating on ethanol fuel through internal reforming at intermediate temperatures. The effect of the synthesis method on the catalytic activity and carbon deposition properties of the catalyst for ESR was emphasized. The combustion synthesis proved to be highly promising. The combustion-synthesized Ni–Ce$_{0.8}$Zr$_{0.2}$O$_2$ catalyst was finally applied as an anode functional layer in a real SOFC operating on ethanol steam fuel, and promising results were demonstrated.

2. Experimental

2.1. Synthesis and fabrication

Two different methods were used for the synthesis of Ni–Ce$_{0.8}$Zr$_{0.2}$O$_2$ (20 wt.% Ni) catalyst powders. The first method was a solution combustion based on the glycine nitrite process (GNP) [28,29]. The second method was a conventional wet impregnation process (IMP); for a typical synthesis, approximately 2.0 g of the Ce$_{0.8}$Zr$_{0.2}$O$_2$ powder (prepared by the combustion synthesis) was dispersed in an aqueous solution containing a proper amount of nickel nitrate. The suspension was aged for 6 h at room temperature to guarantee the sufficient soaking of the solution into the Ce$_{0.8}$Zr$_{0.2}$O$_2$ powder. Then, it was dried at 100 °C and calcined at 700 °C in air for 4 h. After cooling to room temperature naturally, the samples were ground by hand with the help of an agate mortar and pestle, pressed into disks and fragmented into pellets in 40–60 mesh for later catalytic tests.

The fuel cell materials include a Ba$_{0.5}$Sr$_{0.5}$Co$_{0.8}$Fe$_{0.2}$O$_{3-\delta}$ (BSCF) cathode, a (Y$_2$O$_3$)$_{0.1}$(ZrO$_2$)$_{0.9}$ (YSZ) electrolyte, a Sm$_{0.2}$Ce$_{0.8}$O$_2$ (SDC) interlayer and a NiO + YSZ anode (NiO:YSZ = 60:40, by weight). The BSCF was synthesized using an EDTA–citrate complexing sol–gel

process with metal nitrates (analytical reagents) applied as the raw materials [30], while the NiO and YSZ used for the anode were commercial products (Chengdu Shudu Nano-science Co., Ltd. for NiO and Tosoh for YSZ). The disk-shaped anode substrates were first prepared using a tape-casting technique. The green anode pellets were fired at 1100 °C for 2 h in air to release the organic solvents and to create the proper mechanical strength for the substrate. The YSZ colloidal suspension was prepared by dispersing a fine YSZ powder into a solution of ethylene glycol (5 wt.% solid content) through high-energy ball milling (Fritsch, Pulverisette 6), which was then spray-deposited onto the anode substrates. The obtained green anode-electrolyte dual-layer half-cells were sintered at 1400 °C for 5 h in air. The SDC colloidal suspension was then spray-deposited onto the YSZ electrolyte, which was sintered at 1350 °C for 5 h in air. The BSCF–SDC composite cathode (70:30, by weight) was deposited on the SDC interlayer surface and fired at 1000 °C for 2 h in air. To prepare the catalyst layer, a slurry of the catalyst powder was prepared, which was screen-painted onto the outer surface of the anode layer and sintered at 700 °C for 1 h.

2.2. Catalytic evaluation

The catalytic activity of the various catalysts was tested in a flow-through-type fixed-bed quartz-tube reactor with an inner diameter of approximately 8 mm. Approximately 0.2 g of catalyst particles in the size range of 40–60 mesh were placed in the middle of the reactor, and a K-type thermocouple was inserted into the center of the catalyst bed to detect the temperature of the reaction. The gas flow during the ethanol steam reforming reaction was controlled by an AFC 80MD digital mass flow controller (Qualiflow). Ethanol and water were metered and delivered to an evaporator at 180 °C to achieve complete gasification through the HPLC pumps. Then, ethanol, steam and the dilution gas were delivered to the reactor. The products were analyzed online by a Varian CP-3800 GC, which was equipped with a Hayesep Q, a Poraplot Q, a 5 Å sieve molecular capillary columns, a thermal conductivity detector (TCD) for the separation and detection of H$_2$, O$_2$, CO, CO$_2$ and CH$_4$, and a flame ionization detector (FID) for the detection of the combustible substance. Prior to the reaction, the catalysts were reduced in hydrogen at 650 °C for 1 h. The catalytic reaction was performed at 400–650 °C. During the measurement, the liquid flow rate of ethanol and water was 0.05 ml min^{-1} (EtOH:H$_2$O = 1:8, molar ratio), and helium was applied as a carrier gas at a fixed flow rate of 80 ml min^{-1} [STP]. The conversion of ethanol (X (%)) during the steam reforming was calculated according to Eq. (1). The selectivity of H$_2$ (S_1 (%)), CO (S_2 (%)), CO$_2$ (S_3 (%)) and CH$_4$ (S_4 (%)) was calculated according to Eqs. (2)–(5), respectively:

$$X\ (\%) = \frac{F_{\text{ethanol,in}} - F_{\text{ethanol,out}}}{F_{\text{ethanol,in}}} \times 100 \tag{1}$$

$$S_1\ (\%) = \frac{[\text{H}_2]}{[\text{H}_2] + 2[\text{CH}_4]} \times 100 \tag{2}$$

$$S_2\ (\%) = \frac{[\text{CO}]}{[\text{CO}] + [\text{CO}_2] + [\text{CH}_4]} \times 100 \tag{3}$$

$$S_3(\%) = \frac{[\text{CO}_2]}{[\text{CO}] + [\text{CO}_2] + [\text{CH}_4]} \times 100 \tag{4}$$

$$S_4(\%) = \frac{[\text{CH}_4]}{[\text{CO}] + [\text{CO}_2] + [\text{CH}_4]} \times 100 \tag{5}$$

2.3. Characterization

The hydrogen-temperature-programmed reduction (H$_2$-TPR) was used to identify the chemical interaction between NiO and the support. Approximately 0.03 g of catalyst particles were put in a

U-type quartz reactor with an inner diameter of approximately 3 mm. The sample was pretreated in argon at a flow rate of 30 ml min^{-1} [STP] at 400 °C for 30 min. After cooling to room temperature in argon, the atmosphere was changed to 10 vol.% H$_2$/Ar, and the reactor was programmed to heat to 930 °C at a rate of 10 °C min^{-1}. The hydrogen consumption was monitored by a BELCAT-A apparatus equipped with an *in situ* TCD detector.

To evaluate the coke resistance of the various catalysts, approximately 0.2 g of the reduced catalyst particles were placed in a flow-through-type fixed-bed quartz-tube reactor and treated under EtOH:H$_2$O = 1:8 with a liquid flow rate of 0.05 ml min^{-1} for 6 h at 500 °C and then cooled to room temperature in a helium atmosphere. After the treatment, approximately 0.05 g of powder was placed into a U-type quartz reactor with an inner diameter of approximately 3 mm. Pure oxygen (for the oxygen-temperature-programmed oxidization, O$_2$-TPO) at a flow rate of 20 ml min^{-1} [STP] was then introduced to the top of the reactor. After flowing with the gas at room temperature for approximately 30 min to stabilize the baseline, the reactor was heated to 900 °C at a rate of 10 °C min^{-1}. The deposited carbon on the catalyst surface was gradually oxidized to CO$_2$. The effluent gas from the reactor was connected to a mass spectrometer (MS, Hiden QIC-20) for *in situ* monitoring of CO$_2$.

In the NH$_3$-TPD experiments, the samples were first treated in 10 vol.% H$_2$–Ar at 650 °C for 2 h, cooled to 100 °C, and exposed to 20 vol.% NH$_3$ (30 ml min^{-1}, He in balance) for 30 min. The sample was then purged with Ar at 100 °C for 1 h and heated at 10 °C min^{-1} to 650 °C. The NH$_3$ concentration in the effluent gas was online monitored by a BELCAT-A apparatus equipped with an *in situ* TCD detector.

The CO$_2$-TPD process was performed to test the surface basicity of the catalysts. The samples were first reduced in hydrogen at 650 °C for 1 h, cooled to room temperature under the same atmosphere, and exposed to CO$_2$ (20 ml min^{-1}, STP) for 2 h. The treated samples were purged with Ar at room temperature for 1 h and heated at 10 °C min^{-1} to 800 °C in Ar at 20 ml min^{-1} [STP]. The CO$_2$ signal was monitored and recorded continuously as a function of the temperature by MS.

The phase structures of the various samples were examined by an X-ray diffractometer (XRD, D8 Advance, Bruker, Germany) equipped with a Cu K(radiation ($\lambda = 0.1541$ nm). The BET specific surface area of the catalysts was characterized by the N$_2$ adsorption at liquid nitrogen temperature using a surface area analyzer (BELSORP II, Japan). Prior to the nitrogen adsorption, the sample was degassed at 250 °C for 2.0 h to remove any physically adsorbed species. The surface area was determined from the linear portion of the BET equation. The SEM morphology of the calcined powder of the different catalysts was examined by a field emission scanning electron microscope (FESEM, Hitachi S-4800). The laser Raman spectra of the various catalysts after the treatment in EtOH:H$_2$O = 1:8 atmosphere for 6 h at 500 °C was obtained in an HR800 UV Raman microspectrometer (JOBIN YVON, France) using the green line of an argon laser ($\lambda = 514.53$ nm) as the excitation source.

The *I–V* polarization curves of the fuel cells measured at 550–700 °C were obtained using a Keithley 2420 source meter in the 4-probe mode. During the measurements, hydrogen or EtOH–H$_2$O (2.3:1 molar ratio) gas mixtures were fed into the anode chamber and ambient air was used as the cathode atmosphere. The liquid ethanol–water fuel was vaporized by a water bath (70 °C) and introduced into the anode chamber by nitrogen. The flow rate of hydrogen and nitrogen was kept at 60 ml min^{-1} [STP]. The electrode polarization resistance was investigated by the electrochemical impedance spectroscopy (EIS) measurement using a Solartron 1260 frequency response analyzer in combination with a Solartron 1287 potentiostat. The frequency of the EIS

measurement ranged from 0.1 to 1000 kHz and the signal amplitude was 10 mV. The cross-sectional morphology of the fuel cell was examined by an environmental scanning electron microscope (ESEM, QUANTA-200).

3. Results and discussion

3.1. Basic properties

Fig. 1 shows the room-temperature XRD patterns of the Ni–Ce$_{0.8}$Zr$_{0.2}$O$_2$ catalysts before and after the hydrogen reduction at 650 °C for 1 h. For comparison, the XRD pattern of the Ce$_{0.8}$Zr$_{0.2}$O$_2$ support is also presented. As shown in Fig. 1, all the diffraction peaks of Ce$_{0.8}$Zr$_{0.2}$O$_2$ can be indexed as a cubic fluorite structure, suggesting Zr^{4+} was totally incorporated into the fluorite structure of CeO$_2$ with the formation of a solid solution, which agrees well with the literature results [31,32]. As shown in Fig. 1a, very weak NiO peaks were detected in the XRD patterns of the Ni–Ce$_{0.8}$Zr$_{0.2}$O$_2$ (GNP) catalyst, suggesting the majority of the NiO in the Ni–Ce$_{0.8}$Zr$_{0.2}$O$_2$ (GNP) catalyst most likely interacted strongly with the support. However, an appreciable amount of the NiO crystalline phase was observed in the IMP-prepared catalyst. The XRD patterns of the reduced Ni–Ce$_{0.8}$Zr$_{0.2}$O$_2$ catalysts are depicted in Fig. 1b. Diffraction peaks attributed to the Ni phase (44.5° and 51.8°) were observed; however, compared to the Ni–Ce$_{0.8}$Zr$_{0.2}$O$_2$ (IMP), the Ni–Ce$_{0.8}$Zr$_{0.2}$O$_2$ (GNP) showed much weaker and broader diffraction peaks of the metallic nickel phase, suggesting much smaller Ni particle sizes.
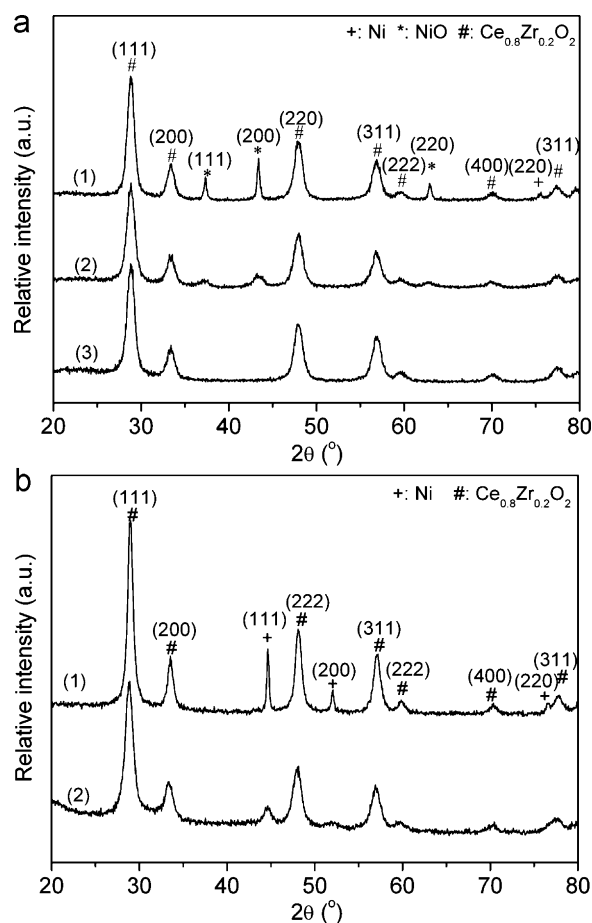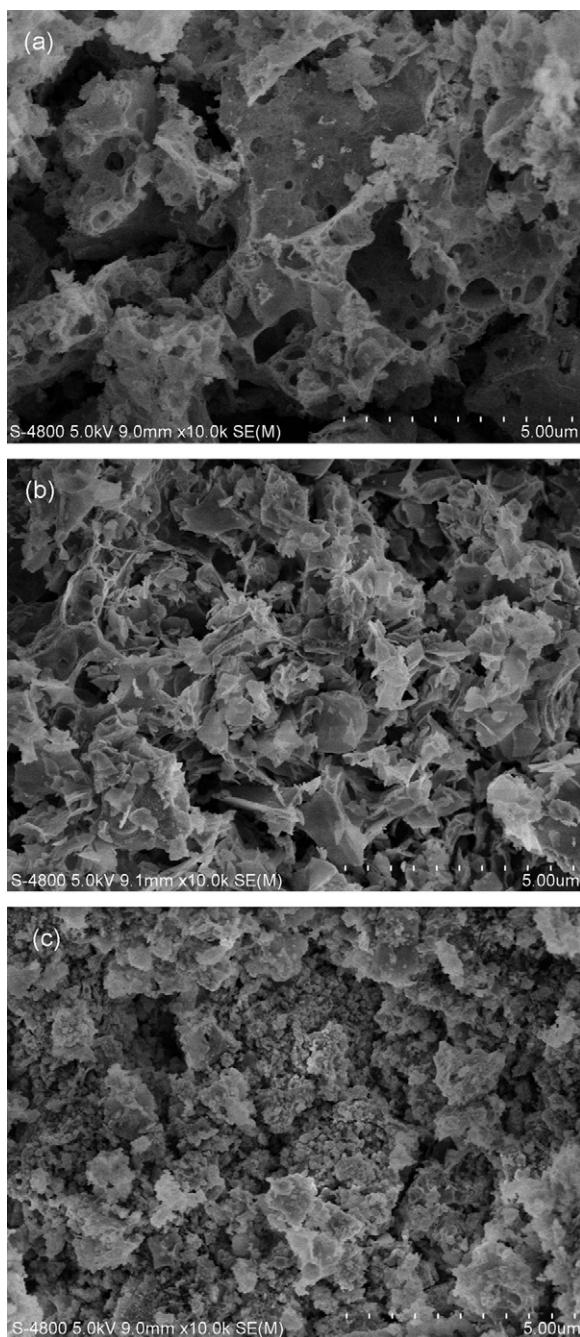

Fig. 1. XRD patterns of the various catalysts before (a) and after (b) the hydrogen reduction after calcination at 700 °C. (1) Ni–Ce$_{0.8}$Zr$_{0.2}$O$_2$ (IMP), (2) Ni–Ce$_{0.8}$Zr$_{0.2}$O$_2$ (GNP) and (3) Ce$_{0.8}$Zr$_{0.2}$O$_2$.

Fig. 2. SEM images of the various catalysts. (a) $Ce_{0.8}Zr_{0.2}O_2$, (b) $NiO–Ce_{0.8}Zr_{0.2}O_2$ (GNP) and (c) $NiO–Ce_{0.8}Zr_{0.2}O_2$ (IMP).

The specific surface area was 32.8, 18.2 and 25.4 $m^2\,g^{-1}$ for $Ce_{0.8}Zr_{0.2}O_2$, $NiO–Ce_{0.8}Zr_{0.2}O_2$ (GNP) and $NiO–Ce_{0.8}Zr_{0.2}O_2$ (IMP), respectively. The nickel oxide likely acted as a catalyst for the combustion reaction and resulted in the more sintered $NiO–Ce_{0.8}Zr_{0.2}O_2$ (GNP). The SEM morphology of the catalysts and the $Ce_{0.8}Zr_{0.2}O_2$ support are shown in Fig. 2. $Ce_{0.8}Zr_{0.2}O_2$ and $NiO–Ce_{0.8}Zr_{0.2}O_2$ (GNP) exhibited porous, sponge-like structures. During the glycine combustion reaction, the emission of large volumes of gas products (N_2, CO_2, H_2O) resulted in the fragile and porous structure of the solid product. However, for the $NiO–Ce_{0.8}Zr_{0.2}O_2$ (IMP) catalyst, NiO was impregnated into the pores of the support, and consequently, the porosity was much reduced. The minor difference in the surface area of $NiO–Ce_{0.8}Zr_{0.2}O_2$ (IMP) and the $Ce_{0.8}Zr_{0.2}O_2$ support implies the nickel oxide mainly occupied the macropores in the support.
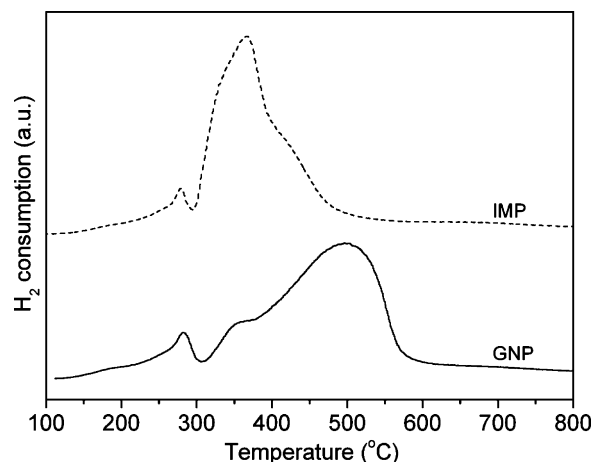
Fig. 3. H_2-TPR profiles of the various $Ni–Ce_{0.8}Zr_{0.2}O_2$ catalysts.

In addition to the surface area, the activity of nickel-based catalysts is also closely related to the interaction of the nickel with the support [33]. The chemical interaction between the nickel and the support was characterized by H_2-TPR, and the profiles are shown in Fig. 3. The peak temperature of free NiO during the H_2-TPR process was reported to be around 330 °C [34]. With the increase in the chemical interaction between NiO and the support, a shift in the reduction peak to higher temperatures is expected. As can be seen, $Ni–Ce_{0.8}Zr_{0.2}O_2$ (IMP) demonstrated a weaker chemical interaction than $Ni–Ce_{0.8}Zr_{0.2}O_2$ (GNP) because the temperature of the main reduction peak was 367 °C, which was lower than 498 °C for $Ni–Ce_{0.8}Zr_{0.2}O_2$ (GNP). There was a considerable amount of free NiO present in $Ni–Ce_{0.8}Zr_{0.2}O_2$ (IMP), while most of the NiO in the $Ni–Ce_{0.8}Zr_{0.2}O_2$ (GNP) catalyst interacted with the $Ce_{0.8}Zr_{0.2}O_2$ support, which agrees well with the XRD results. According to the H_2-TPR results, the larger the particle sizes led to the easier reduction of the nickel oxide [35]. The interaction between NiO and the support strongly affected the Ni particle size, consequently, the catalytic activity. This interaction would prevent the mobility of the Ni^{2+} on the support surface at higher temperatures. Thus, the metals that have strong interactions with the support typically should have a high resistance to be sintered and a higher dispersion.

Another important factor in determining the catalytic activity of nickel is its crystalline size. The crystalline size of the metallic nickel in $Ni–Ce_{0.8}Zr_{0.2}O_2$ (GNP) and $Ni–Ce_{0.8}Zr_{0.2}O_2$ (IMP), as calculated from the XRD diffraction peak at $2\theta = 51.8°$ using the Scherrer equation, was 8.7 nm and 26.5 nm, respectively. The difference in the crystalline size of the metallic nickel should be attributed to the different preparation methods. The strong interaction of the NiO species with the support phase, as evidenced by the H_2-TPR and powder XRD, and higher metallic dispersion contributed greatly to the fine crystalline size of the nickel in the $Ni–Ce_{0.8}Zr_{0.2}O_2$ (GNP) catalyst. The small Ni particle size would be beneficial for the suppression of carbon deposition over the catalyst during the ESR.

3.2. Catalytic performance

The effect of the reaction temperature on the catalytic performance was investigated at a steam-to-carbon feed ratio (mol mol^{-1}) of 4.0, atmospheric pressure and temperatures in the range of 400–650 °C, the results of which are shown in Fig. 4. Both catalysts showed good catalytic activity for the ESR; the complete ethanol conversion was achieved at a temperature as low as 400 °C. For the catalysts, the main products were H_2, CO, CH_4 and CO_2, while only minor amounts of byproducts, such as CH_3CHO and CH_3COCH_3, were detected by applying the $Ni–Ce_{0.8}Zr_{0.2}O_2$ (IMP) catalyst.
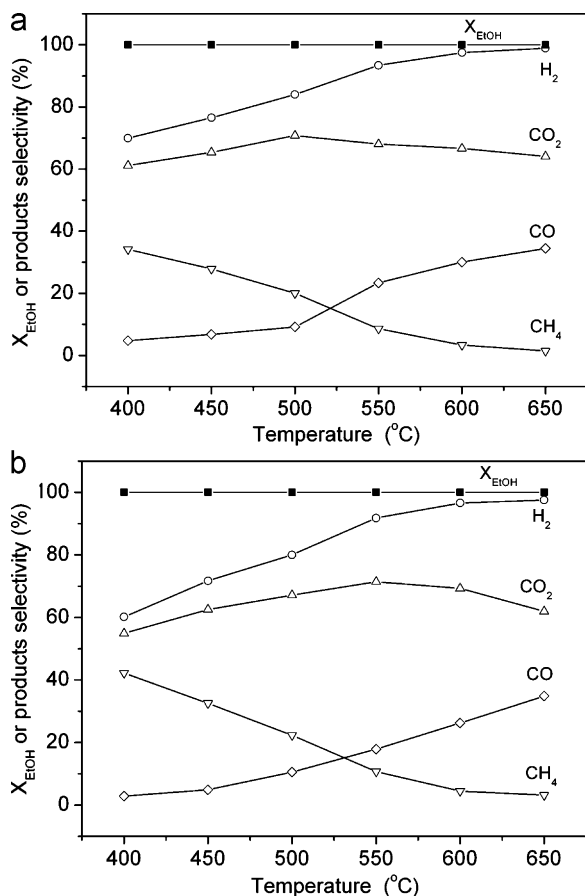
Fig. 4. Catalytic activity of the (a) $Ni-Ce_{0.8}Zr_{0.2}O_2$ (GNP) and (b) $Ni-Ce_{0.8}Zr_{0.2}O_2$ (IMP) catalysts for ethanol steam reforming ($EtOH:H_2O = 1:8$).
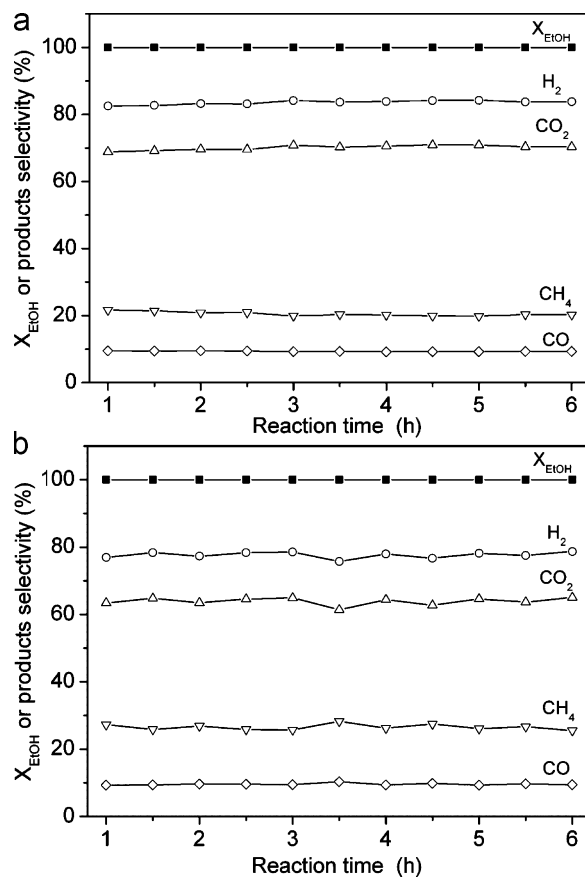
Fig. 5. The time dependence on the conversion of ethanol and the selectivity of various products over different catalysts: (a) $Ni-Ce_{0.8}Zr_{0.2}O_2$ (GNP) and (b) $Ni-Ce_{0.8}Zr_{0.2}O_2$ (IMP).

Previous investigations of the reaction mechanism of the partial oxidation of ethanol or of ethanol steam reforming over $M-CeO_2$ catalysts suggested that the ethoxy species probably acted as the reaction intermediate. In addition, the rate for the decomposition of the intermediate may be faster than that for the ethanol decomposition into acetaldehyde, as reported by Morgenstern and Fornango [36]. Increasing the reaction temperature led to a higher H_2 yield and selectivity but a lower methane selectivity. This result suggested that the steam reforming of methane, which is thermodynamically feasible, occurred as the major reaction. However, the CO selectivity decreased due to the intrinsically unfavorable effect of temperature on the WGS reaction. For instance, increasing the reaction temperature from 400 to 600 °C enhanced the hydrogen selectivity from 70.0% to 97.5% over $Ni-Ce_{0.8}Zr_{0.2}O_2$ (GNP) and the CO selectivity from 4.7 to 30.0%.

Both catalysts presented a high and comparable H_2 selectivity above 600 °C. However, a decrease in the operational temperature led to different activities. The H_2 selectivity of $Ni-Ce_{0.8}Zr_{0.2}O_2$ (GNP) and $Ni-Ce_{0.8}Zr_{0.2}O_2$ (IMP) at 550 °C was 93.4% and 91.8%, respectively. There was an obvious diversity in the H_2 selectivity of the catalysts when the reaction temperature was reduced to below 450 °C. The H_2 selectivity of $Ni-Ce_{0.8}Zr_{0.2}O_2$ (GNP) and $Ni-Ce_{0.8}Zr_{0.2}O_2$ (IMP) at 400 °C was 70.0% and 60.2%, respectively. The CH_4 selectivity over $Ni-Ce_{0.8}Zr_{0.2}O_2$ (GNP) was lower than that of $Ni-Ce_{0.8}Zr_{0.2}O_2$ (IMP). These results indicated that $Ni-Ce_{0.8}Zr_{0.2}O_2$ (GNP) was more active than the $Ni-Ce_{0.8}Zr_{0.2}O_2$ (IMP) catalyst for the methane steam reforming reaction at 400–650 °C.

3.3. Catalytic stability and carbon deposition

The stability of both catalysts for ESR was investigated at 500 °C using a liquid flow rate of ethanol–water mixtures of 0.05 ml min^{-1} ($EtOH:H_2O = 1:8$, molar ratio) and a flow rate of the diluting helium gas of 80 ml min^{-1} [STP], and the results are shown in Fig. 5. During the test period of approximately 6 h, the ethanol conversion was maintained at 100% for both catalysts; however, the selectivity of the products showed substantially different changes. The $Ni-Ce_{0.8}Zr_{0.2}O_2$ (GNP) was superior to $Ni-Ce_{0.8}Zr_{0.2}O_2$ (IMP) in hydrogen selectivity, agreeing well with our previous catalytic activity results. The methane selectivity of $Ni-Ce_{0.8}Zr_{0.2}O_2$ (GNP) was relatively lower than that of $Ni-Ce_{0.8}Zr_{0.2}O_2$ (IMP). The $Ni-Ce_{0.8}Zr_{0.2}O_2$ (GNP) catalyst showed good stability for the selectivity of the products, while the product selectivity fluctuated with increasing the operation time of the $Ni-Ce_{0.8}Zr_{0.2}O_2$ (IMP) catalyst.

The catalytic stability for ESR is closely related to coke formation over the catalyst. After the stability test, the catalyst was cooled down to room temperature in a helium flux and characterized by O_2-TPO to analyze the carbon deposition properties. Fig. 6 shows the corresponding O_2-TPO profiles of the catalysts after treatment in $EtOH:H_2O = 1:8$ for 6 h. The CO_2 peak areas were calculated as 4.47×10^{-7} and 1.19×10^{-6} for $Ni-Ce_{0.8}Zr_{0.2}O_2$ (GNP) and $Ni-Ce_{0.8}Zr_{0.2}O_2$ (IMP), respectively. The CO_2 peak area reflects the amount of carbon deposited on the catalysts. These results suggested that the $Ni-Ce_{0.8}Zr_{0.2}O_2$ (GNP) showed a much better coke resistance towards the ethanol steam reforming, which was in good agreement with the results of the Ni particle sizes evidenced by XRD and the methane selectivity in the catalytic activity test.
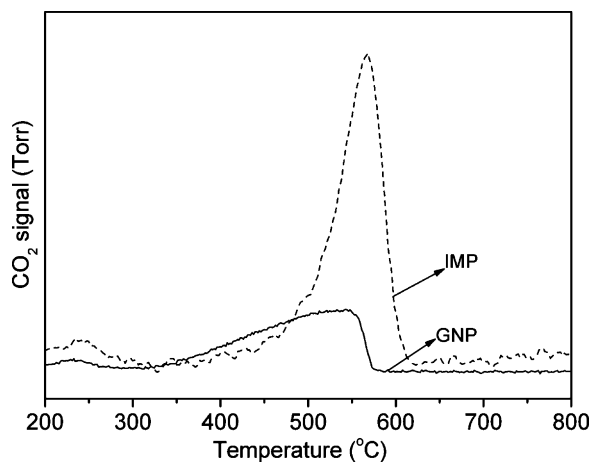
Fig. 6. O_2-TPO profiles of the various $Ni–Ce_{0.8}Zr_{0.2}O_2$ catalysts after treatment in EtOH:H_2O = 1:8 for 5 h at 500 °C.
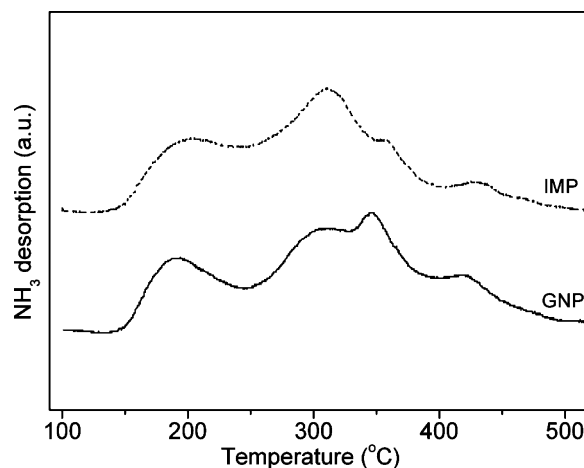

Fig. 8. The NH_3-TPD profiles of the various $Ni–Ce_{0.8}Zr_{0.2}O_2$ catalysts.
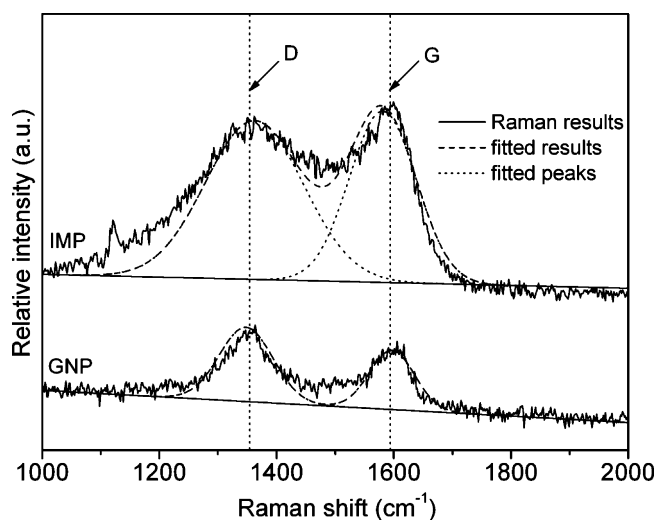

Fig. 7. Raman spectra of the deposited carbon on the various $Ni–Ce_{0.8}Zr_{0.2}O_2$ catalysts after treatment in EtOH:H_2O = 1:8 for 5 h at 500 °C.

Fig. 9. The CO_2-TPD profiles of the various $Ni–Ce_{0.8}Zr_{0.2}O_2$ catalysts.

To investigate the structures of the deposited carbon, laser Raman spectra of the two carbon-deposited catalysts were measured. As shown in Fig. 7, the Raman spectra showed two intense bands: at 1350 cm^{-1} (usually called the D-band), which is associated with the disordered structure of carbon and one at 1580 cm^{-1} (usually called the G-band), which is assigned to the in-plane vibrations of the carbon atoms in hexagonal sheets [37]. The graphitization degree of the deposited carbon was related to the integrated intensity ratio in the form of R (I_D/I_G) [38]. According to the literature, the R-values should decrease with the increasing carbon graphitization degree [39]. The R-values of the deposited carbon over the $Ni–Ce_{0.8}Zr_{0.2}O_2$ (GNP) and $Ni–Ce_{0.8}Zr_{0.2}O_2$ (IMP) were 1.59 and 1.36, respectively. This result implies the graphitization degree of the carbon deposited over $Ni–Ce_{0.8}Zr_{0.2}O_2$ (GNP) is much lower than that over $Ni–Ce_{0.8}Zr_{0.2}O_2$ (IMP). That is, the carbon deposited over the $Ni–Ce_{0.8}Zr_{0.2}O_2$ (GNP) should be much easier to eliminate as compared to that deposited over the $Ni–Ce_{0.8}Zr_{0.2}O_2$ (IMP).

An acidic catalyst surface favors carbon deposition, whereas a basic one suppresses carbon deposition [40]. The NH_3-TPD patterns of the various $Ni–Ce_{0.8}Zr_{0.2}O_2$ catalysts are shown in Fig. 8. For both samples, the acidic sites are distributed in three desorption regions at 150–250, 250–400 and 400–500 °C, which are labeled as α, β and γ peaks and associated with weak, medium and strong acid sites,

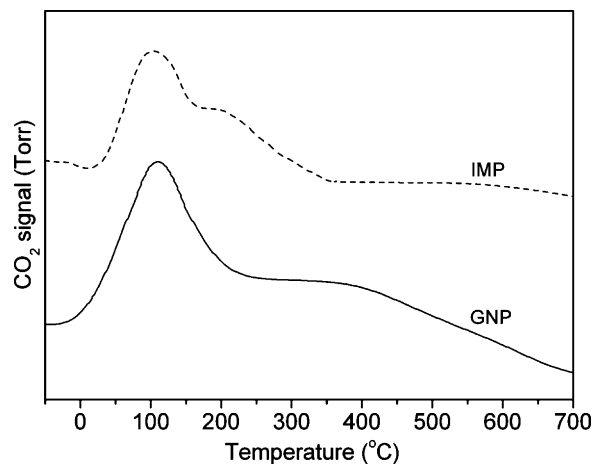respectively. The α peak was assigned to the physical adsorption of NH_3 or the interaction between NH_3 and the surface oxides or hydroxyl groups [41]. The β peak should be attributed to the acidic hydroxyl group with weak acid sites [42]. The γ peak corresponded to the strong Lewis and/or Brönsted acid sites [41]. All the tested samples showed similar acid site distributions, but different concentrations were observed. As can be seen, the intensity of the α peak of $Ni–Ce_{0.8}Zr_{0.2}O_2$ (GNP) was relatively higher than that of $Ni–Ce_{0.8}Zr_{0.2}O_2$ (IMP). The results suggested that $Ni–Ce_{0.8}Zr_{0.2}O_2$ (GNP) had more weak acid sites on the catalyst surface, which is helpful for the adsorption and activation of methane. The intensity of the β peak of $Ni–Ce_{0.8}Zr_{0.2}O_2$ (GNP) was relatively lower than that of $Ni–Ce_{0.8}Zr_{0.2}O_2$ (IMP), suggesting the $Ni–Ce_{0.8}Zr_{0.2}O_2$ (IMP) presented more strong acid sites than that of $Ni–Ce_{0.8}Zr_{0.2}O_2$ (GNP). As can be seen, the intensity of the γ peak was almost the same for both catalysts. This result indicated that the number of strong Lewis and/or Brönsted acid sites was comparable for both catalysts. The temperatures of the different peaks of $Ni–Ce_{0.8}Zr_{0.2}O_2$ (GNP) were relatively lower than that of $Ni–Ce_{0.8}Zr_{0.2}O_2$ (IMP). This suggested that the strength of the acidic sites of $Ni–Ce_{0.8}Zr_{0.2}O_2$ (GNP) was lower than that of $Ni–Ce_{0.8}Zr_{0.2}O_2$ (IMP), which explained the better coke resistance of the GNP-prepared catalyst.

To test the surface basicity of the $Ni–Ce_{0.8}Zr_{0.2}O_2$ catalysts, the CO_2-TPD analysis was performed. Fig. 9 shows the corresponding CO_2-TPD profiles of the $Ni–Ce_{0.8}Zr_{0.2}O_2$ (GNP) and $Ni–Ce_{0.8}Zr_{0.2}O_2$ (IMP) catalysts. No absorption peak appeared above 700 °C,

implying that no carbonate was formed in the CO_2-TPD process. There were two peaks in the CO_2-TPD profiles of both catalysts. The Ni–$Ce_{0.8}Zr_{0.2}O_2$ (IMP) showed desorption peaks at 100 and 198 °C. Similar to Ni–$Ce_{0.8}Zr_{0.2}O_2$ (IMP), Ni–$Ce_{0.8}Zr_{0.2}O_2$ (GNP) had one desorption peak near 100 °C with high peak intensity. The other peak with weak intensity appeared near 360 °C. However, the intensity of the two peaks of Ni–$Ce_{0.8}Zr_{0.2}O_2$ (GNP) was higher than that of Ni–$Ce_{0.8}Zr_{0.2}O_2$ (IMP), suggesting that there are more weak and medium basic sites present in the Ni–$Ce_{0.8}Zr_{0.2}O_2$ (GNP) catalyst. The CO_2 peak areas were 1.07×10^{-7} and 5.58×10^{-8} for the Ni–$Ce_{0.8}Zr_{0.2}O_2$ (GNP) and Ni–$Ce_{0.8}Zr_{0.2}O_2$ (IMP), respectively. Thus, the Ni–$Ce_{0.8}Zr_{0.2}O_2$ (GNP) catalyst had a higher surface basicity than the Ni–$Ce_{0.8}Zr_{0.2}O_2$ (IMP). This result showed that the good coke resistance of the Ni–$Ce_{0.8}Zr_{0.2}O_2$ (GNP) should be attributable to the smaller crystalline size of nickel, the strong chemical interaction and the large surface basicity of the catalyst.

3.4. Performance in a single cell

The Ni–$Ce_{0.8}Zr_{0.2}O_2$ (GNP) catalyst was also exploited as the anode functional layer in a real fuel cell. The catalyst layer was fabricated over the anode at 700 °C. Shown in Fig. 10a and b are the *I–V* and *I–P* curves of the fuel cells with the Ni–$Ce_{0.8}Zr_{0.2}O_2$ (GNP) catalyst layer operating on hydrogen and EtOH–H_2O gas mixtures at different temperatures. When operating on the EtOH–H_2O gas mixtures, the peak power densities were 536, 334, 162 and 74 mW cm^{-2} at 700, 650, 600 and 550 °C, respectively, and they were 755, 488, 262 and 125 mW cm^{-2} when operating on hydrogen fuel. These results indicated that the power outputs of the cell operating on EtOH–H_2O are only slightly lower than that of hydrogen fuel. To properly determine the difference of the cell performances with hydrogen and EtOH–H_2O fuels, the cell impedance

operated on the two fuels under OCV conditions was also measured, the results of which are shown in Fig. 10c and d. At the same furnace temperature, the electrolyte resistance of the cell operating on EtOH–H_2O seemed be higher than that of hydrogen. For example, it was 0.23 Ω cm^{-2} at 700 °C when applying the hydrogen fuel and it was 0.26 Ω cm^{-2} for EtOH–H_2O. This result suggested that the real cell temperature when applying the EtOH–H_2O fuel might be slightly lower than the furnace temperature. The ESR is endothermic in nature. Thus, the fuel cell temperature could be slightly lower than the set temperature; consequently, lower peak power densities were achieved.

For comparison, the carbon deposition and cell performance of a cell with a conventional Ni–YSZ anode was also investigated. After the treatment in the EtOH:H_2O = 1:8 atmosphere for 6 h at 500 °C, the carbon-deposited catalyst was then conducted to the O_2-TPO analysis. The CO_2 peak area was calculated as 3.32×10^{-5}, which was more than 75 times that of Ni–$Ce_{0.8}Zr_{0.2}O_2$ (GNP). Shown in Fig. 11 are the *I–V* and *I–P* curves of the fuel cells without a catalyst layer operating on hydrogen and EtOH–H_2O gas mixtures at different temperatures. When operating on H_2 fuel, the PPDs were 735, 490, 275 and 140 mW cm^{-2} at 700, 650, 600 and 550 °C, respectively. The PPDs of the cell without a catalyst layer were similar to that of the cell with a catalyst layer. When operating on the EtOH–H_2O gas mixtures, the PPDs were 626 and 386 mW cm^{-2} at 700 and 650 °C, respectively. When the furnace temperature decreased to 600 °C, the OCV and PPD were 0.837 V and 20 mW cm^{-2}, respectively. After the test, the cell was protected in hydrogen and cooled to room temperature. It was found that the cell was significantly destroyed by the deposited carbon that covered the entire anode surface. Those results suggested that the Ni–$Ce_{0.8}Zr_{0.2}O_2$ (GNP) catalyst layer successfully protected the anode from serious carbon deposition under the operation on ethanol steam fuel [43].
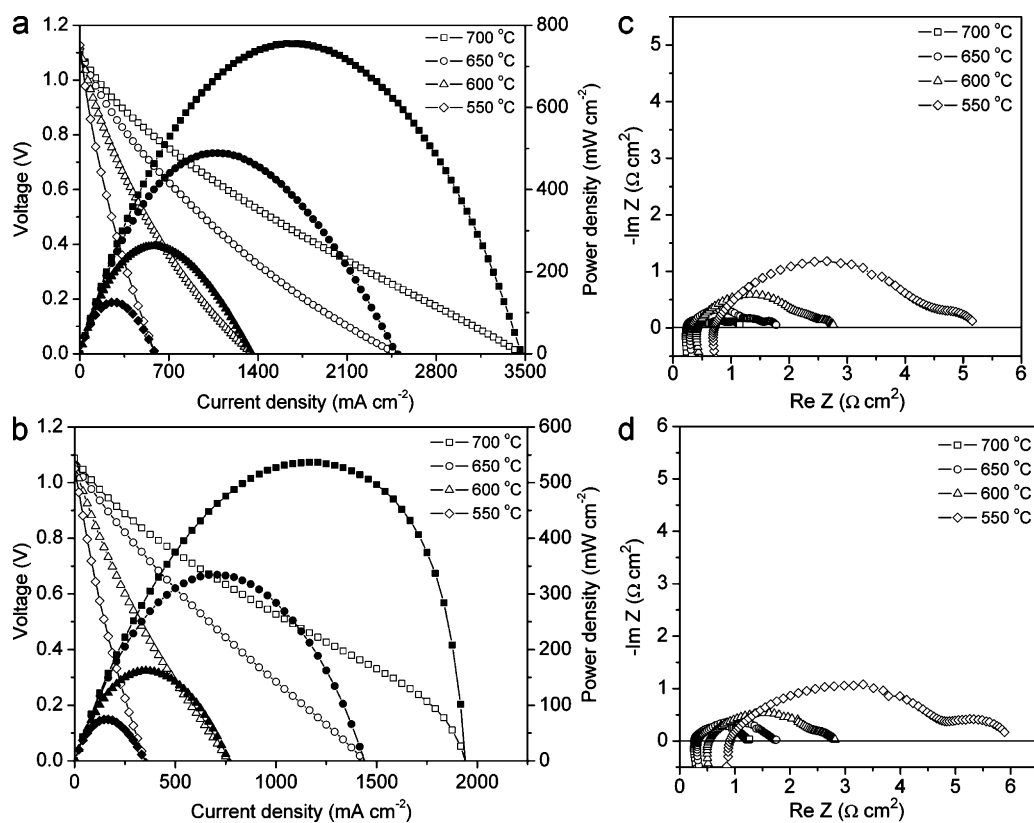
Fig. 10. *I–V* and *I–P* curves and the impedance spectra of the fuel cell with the Ni–$Ce_{0.8}Zr_{0.2}O_2$ (GNP) catalyst layer operating on a mixed gas composed of hydrogen (a and c) and 69.7% EtOH and 30.3% H_2O (b and d) at different temperatures.
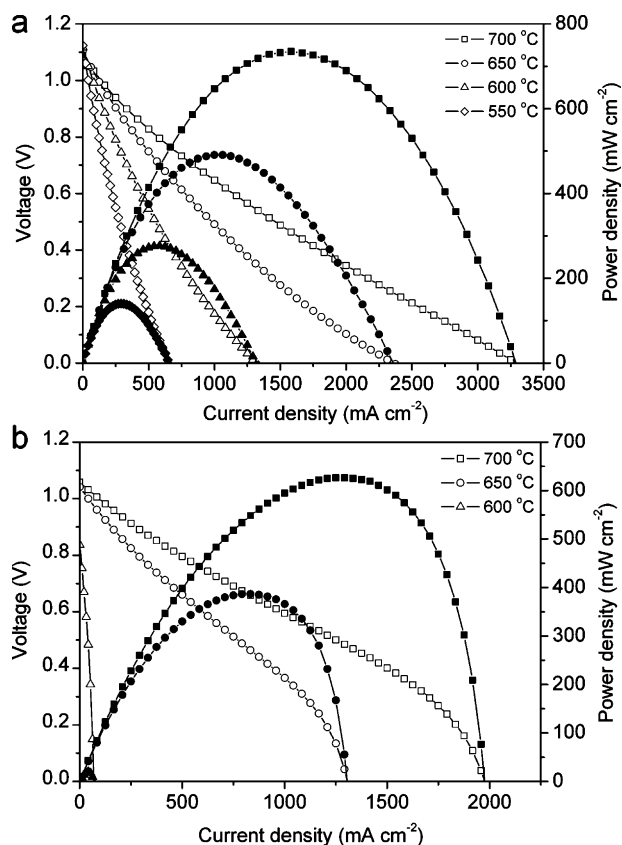
Fig. 11. *I–V* and *I–P* curves of the fuel cell without the catalyst layer operating on a mixed gas composed of (a) hydrogen and (b) 69.7% EtOH and 30.3% H_2O at different temperatures.
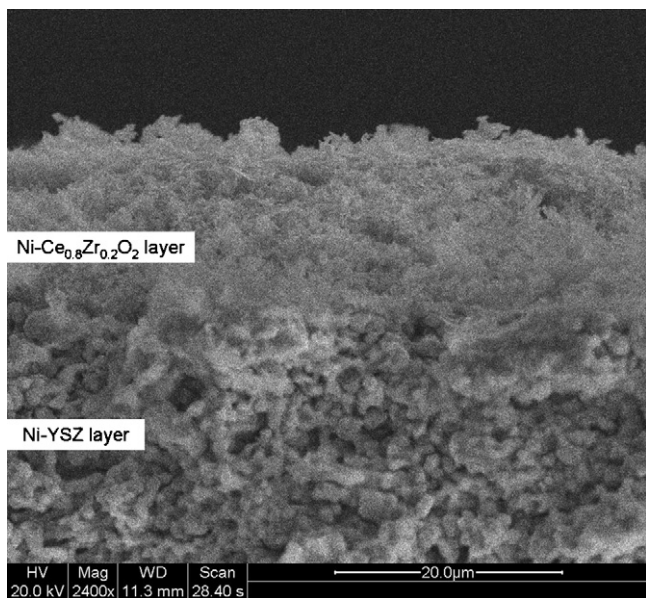
Fig. 12. Cross-sectional SEM image of the catalyst–anode interface.

The SEM image of the fresh fuel cell is shown in Fig. 12. The catalyst layer adhered to the anode surface fairly well. The above results indicated that the Ni–$Ce_{0.8}Zr_{0.2}O_2$ (GNP) catalyst can be ideally used as the catalyst layer of SOFCs operating on ethanol steam fuel.

4. Conclusions

The combustion-synthesized Ni–$Ce_{0.8}Zr_{0.2}O_2$ catalyst had good catalytic activity for ESR between 400 and 650 °C, and it was superior to a similar catalyst prepared by IMP. The strong interaction between NiO and the support accounted for the high activity of the Ni–$Ce_{0.8}Zr_{0.2}O_2$ (GNP) catalyst. Ni–$Ce_{0.8}Zr_{0.2}O_2$ (GNP) also had a better initial stability at 500 °C and a much better coking resistance than Ni–$Ce_{0.8}Zr_{0.2}O_2$ (IMP). The strong interaction between NiO and $Ce_{0.8}Zr_{0.2}O_2$, the smaller nickel particle size and the relatively lower methane selectivity in the products should account for the better coking resistance of the Ni–$Ce_{0.8}Zr_{0.2}O_2$ (GNP) over Ni–$Ce_{0.8}Zr_{0.2}O_2$ (IMP). Ni–$Ce_{0.8}Zr_{0.2}O_2$ (GNP) also showed a lower graphitization degree of the deposited carbon than Ni–$Ce_{0.8}Zr_{0.2}O_2$ (IMP). The excellent catalytic activity of Ni–$Ce_{0.8}Zr_{0.2}O_2$ (GNP) for ethanol conversion to hydrogen resulted in the high cell performance of the fuel cell with this catalyst as the anode catalyst layer operating on EtOH–H_2O gas mixtures. The low price of Ni–$Ce_{0.8}Zr_{0.2}O_2$ (GNP), its good catalytic activity and stability and high coking resistance demonstrate high promise for its application as the catalyst layer in solid oxide fuel cells operating on ethanol steam fuel.

References

[1] J.P. Breen, R. Burch, H.M. Coleman, Appl. Catal. B: Environ. 39 (2002) 65–74.
[2] F. Frusteri, S. Freni, L. Spadaro, V. Chiodo, G. Bonura, S. Donato, S. Cavallaro, Catal. Commun. 5 (2004) 611–615.
[3] T. Hibino, A. Hashimoto, T. Inoue, J. Tokuno, S. Yoshida, M. Sano, Science 288 (2000) 2031–2033.
[4] S. Park, J.M. Vohs, R.J. Gorte, Nature 404 (2000) 265–267.
[5] A. Wojcik, H. Middleton, I. Damopoulos, J. Van herle, J. Power Sources 118 (2003) 342–348.
[6] Y.Z. Wu, C. Su, C.M. Zhang, R. Ran, Z.P. Shao, Electrochem. Commun. 11 (2009) 1265–1268.
[7] C. Su, Y.Z. Wu, W. Wang, Y. Zheng, R. Ran, Z.P. Shao, J. Power Sources 195 (2010) 1333–1343.
[8] Z.L. Zhan, S.A. Barnett, Science 308 (2005) 844–847.
[9] Z.L. Zhan, S.A. Barnett, Solid State Ionics 176 (2005) 871–879.
[10] Z.L. Zhan, Y.B. Lin, M. Pillai, I. Kim, S.A. Barnett, J. Power Sources 161 (2006) 460–465.
[11] D.K. Liguras, D.I. Kondarides, X.E. Verykios, Appl. Catal. B: Environ. 43 (2003) 345–354.
[12] V. Fierro, O. Akdim, H. Provendier, C. Mirodatos, J. Power Sources 145 (2005) 659–666.
[13] F. Aupêtre, C. Descorme, D. Duprez, Catal. Commun. 3 (2002) 263–267.
[14] S. Cavallaro, V. Chiodo, A. Vita, S. Freni, J. Power Sources 123 (2003) 10–16.
[15] P. Biswas, D. Kunzru, Catal. Lett. 118 (2007) 36–49.
[16] S.B. Wang, G.Q. Lu, Appl. Catal. A: Gen. 169 (1998) 271–280.
[17] E. Ruckenstein, Y.H. Hu, Appl. Catal. A: Gen. 133 (1995) 149–161.
[18] J.B. Wang, Y.L. Tai, W.P. Dow, T.J. Huang, Appl. Catal. A: Gen. 218 (2001) 69–79.
[19] A. Trovarelli, C. de Leitenburg, M. Boaro, G. Dolcetti, Catal. Today 50 (1999) 353–367.
[20] A. Trovarelli, Catal. Rev. Sci. Eng. 38 (1996) 439–520.
[21] G. Colón, M. Pijolat, F. Valdivieso, H. Vidal, J. Kašpar, E. Finocchio, M. Daturi, C. Binet, J.C. Lavalley, R.T. Baker, S. Bernal, J. Chem. Soc. Faraday Trans. 94 (1998) 3717–3726.
[22] G. Colón, F. Valdivieso, M. Pijolat, R.T. Baker, J.J. Calvino, S. Bernal, Catal. Today 50 (1999) 271–284.
[23] J. Kašpar, P. Fornasiero, M. Graziani, Catal. Today 50 (1999) 285–298.
[24] S. Rossignol, F. Gérard, D. Duprez, J. Mater. Chem. 9 (1999) 1615–1620.
[25] P. Biswas, D. Kunzru, Int. J. Hydrogen Energy 32 (2007) 969–980.
[26] C. Diagne, H. Idriss, K. Pearson, M.A. Gómez-García, A. Kiennemann, C. R. Chim. 7 (2004) 617–622.
[27] Y.Z. Chen, Z.P. Shao, N.P. Xu, Energy Fuels 22 (2008) 1873–1879.

[28] W. Wang, W. Zhou, R. Ran, R. Cai, Z.P. Shao, Electrochem. Commun. 11 (2009) 194–197.
[29] W. Wang, R. Ran, Z.P. Shao, J. Power Sources 196 (2011) 90–97.
[30] H.X. Gu, R. Ran, W. Zhou, Z.P. Shao, J. Power Sources 172 (2007) 704–712.
[31] J.A. Montoya, E. Romero-Pascual, C. Gimon, P. Del Angel, A. Monzón, Catal. Today 63 (2000) 71–85.
[32] M.H. Youn, J.G. Seo, K.M. Cho, S.Y. Park, D.R. Park, J.C. Jung, I.K. Song, Int. J. Hydrogen Energy 33 (2008) 5052–5059.
[33] S. Takenaka, H. Umebayashi, E. Tanabe, H. Matsune, M. Kishida, J. Catal. 245 (2007) 392–400.
[34] S.D. Robertson, B.D. McNicol, H. De Bass, S.C. Kloet, J.W. Jenkins, J. Catal. 37 (1975) 424–431.
[35] J.J. Guo, H. Lou, H. Zhao, D.F. Chai, X.M. Zheng, Appl. Catal. A: Gen. 273 (2004) 75–82.
[36] D.A. Morgenstern, J.P. Fornango, Energy Fuels 19 (2005) 1708–1716.
[37] F. Tuinstra, J.L. Koenig, J. Chem. Phys. 53 (1970) 1126–1130.
[38] A. Cuesta, P. Dhamelincourt, J. Laureyns, A. Martínez-Alonso, J.M.D. Tascón, Carbon 32 (1994) 1523–1532.
[39] P. Lespade, A. Marchand, M. Couzi, F. Cruege, Carbon 22 (1984) 375–385.
[40] S.B. Tang, F.L. Qiu, S.J. Lu, Catal. Today 24 (1995) 253–255.
[41] N.Y. Topsøe, K. Pedersen, E.G. Derouane, J. Catal. 70 (1981) 41–52.
[42] C.V. Hidalgo, H. Itoh, T. Hattori, M. Niwa, Y. Murakami, J. Catal. 85 (1984) 362–369.
[43] W. Wang, C. Su, Y.Z. Wu, R. Ran, Z.P. Shao, J. Power Sources 195 (2010) 402–411.